The dependence of $\nu_{C=O}$ on the electronegativity of X is seen in the data of Table III for 10-S-4 sulfuranes,[34] 10-I-3 iodinanes,[11,34,35] 10-I-4 iodinane oxide,[36] and 12-I-5 periodinanes.[11] The 10-S-4 sulfuranes clearly have a more polarizable three-center hypervalent bond than the 10-I-3 analogues. The low frequencies of $\nu_{C=O}$ for **26** (1617 cm^{-1}) and **27** (1595 cm^{-1}) suggest that since both have frequencies near that of a carboxylate anion, the endocyclic I–O bond is indeed a very weak one, as already suggested by the NMR chemical shifts of their ortho protons.

The reported[30] catalytic action of **26** or **27** in hydrolyses of phosphate or carboxylate esters is indeed likely to proceed by an initial nucleophilic attack of the apical oxygen of the iodine of **26** or **27** at the electrophilic center of the ester. The evidence which we have interpreted in terms of weak bonding between iodine and the ortho carboxylate substituent might initially lead one to suspect that the apical oxygen should not be strongly nucleophilic. As the transition state forms a bond to the electrophilic ester, however, the increased strength of bonding to the ortho carboxylate oxygen in the more symmetrical three-center O–I–O bond of the transition state lowers the energy of activation for the catalysis by **26** or **27**. This would not occur for an iodosoarene or iodoxyarene lacking the ortho carboxylate substituent.

Conclusion

The lack of reactivity of the periodonium ion of **1a** is better rationalized by comparison with other spirobicyclic 10-X-4 systems than with other known 12-I-5 or 10-I-4 species. Striking parallels between the structures and properties of 10-X-4 species with identical bidentate ligands, including periodonium cation **1a** (10-I-4), phosphoranide anion **18** (10-P-4), and neutral sulfurane **19a** (10-S-4), support the idea[9a] that properties of isovalent and isostructural hypervalent 10-X-4 species are predictable on the basis of ligand properties. Indeed the most striking aspect of the reactivity of the periodonium ion of **1a** is how little it resembles the reactivity of other known iodine species in the same oxidation state. This is a direct result of the specific geometry and electron distribution imposed on the central atom of a 10-X-4 species by the spirobicyclic ligand system, which was designed for specific stabilizing features for Ψ-TBP and TBP 10-X-L systems.

Acknowledgment. This research was supported in part by a grant from the National Science Foundation, CHE 81-13142, at the University of Illinois. The Alexander von Humboldt Stiftung, with R. Schmutzler as host of J.C.M. at the Technische Universität, Braunschweig, Germany, provided support during manuscript preparation.

Supplementary Material Available: X-ray structure and listings of coordinates, thermal parameters, bond lengths, and bond angles for periodonium salt **1a** (8 pages); a listing of observed and calculated structure factors (23 pages). Ordering information is given on any current masthead page.

(35) Etter, M. L. *J. Solid State Chem.* **1976**, *16*, 399.
(36) Bell, R.; Morgan, K. J. *J. Chem. Soc.* **1960**, 1209.

Scanning Tunneling and Atomic Force Microscopy Study of Layered Transition Metal Halides Nb_3X_8 (X = Cl, Br, I)

S. N. Magonov,*,† P. Zönnchen,† H. Rotter,† H.-J. Cantow,† G. Thiele,† J. Ren,‡ and M.-H. Whangbo*,‡

Contribution from the Freiburger Materialsforschungszentrum and Institut für Anorganische und Analytische Chemie. Albert-Ludwigs Universität, D-7800 Freiburg, Germany, and Department of Chemistry, North Carolina State University, Raleigh, North Carolina 27695-8204.
Received September 28, 1992

Abstract: Niobium halides Nb_3X_8 (X = Cl, Br, I) are made up of layers of composition Nb_3X_8, and the two surfaces (A and B) of their individual Nb_3X_8 layers are not equivalent in atomic corrugations. The surfaces of these halides were examined by atomic force microscopy (AFM) and scanning tunneling microscopy (STM) to obtain atomic resolution images. For a given surface, AFM images differ significantly from STM images, and the resolution of the STM images depends on the tunneling conditions. The observed AFM and STM images were analyzed by calculating the total electron density distribution, $\rho(r_0)$, and the partial electron density distribution, $\rho(r_0, e_f)$, for the two surfaces of single Nb_3X_8 (X = Cl, Br, I) layers. Our work shows that the AFM and STM images are well described by the $\rho(r_0)$ and $\rho(r_0, e_f)$ plots, respectively. A combined use of AFM and STM is useful in characterizing the surfaces of layered materials, and calculations of $\rho(r_0)$ and $\rho(r_0, e_f)$ plots are indispensable in interpreting their AFM and STM images.

Introduction

Layered transition metal chalcogenides and halides exhibit interesting physical properties associated with their low-dimensional structures. Individual layers of these compounds have a structure in which a sheet of transition metal atoms is sandwiched between sheets of chalcogen or halogen atoms. Such layers stack to form a three-dimensional structure, with van der Waals (VDW) interactions between adjacent layers. Thus, these compounds are easily cleaved along the layer plane to give clean and flat surfaces and hence are attractive for surface studies with scanning probe techniques. Since the advent of scanning tunneling microscopy (STM)[1,2] and atomic force microscopy (AFM),[3,4] many layered materials have been investigated.

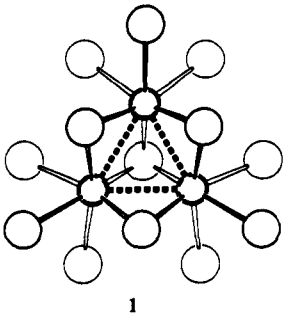

1

† Albert-Ludwigs Universität.
‡ North Carolina State University.

0002-7863/93/1515-2495$04.00/0

In STM applications, atomic resolution images were obtained for several layered compounds,[5-8] and complex patterns associated with charge density waves (CDWs) were visualized.[9] Interpretation of the STM images of layered materials has been carried out largely on the basis of the surface topologies expected from their bulk crystal structures. STM involves electron tunneling either from the surface to the tip or from the tip to the surface. Electrons flow into the lowest unoccupied level of the surface in the tip-to-surface tunneling but leave from the highest occupied level of the surface in the surface-to-tip tunneling. When the tip-to-surface distance r_0 is large, the tip-surface interaction is negligible,[10,11] and the tunneling current (and hence the brightness of an STM image) in the constant-height mode is proportional to $\rho(r_0, e_f)$. The latter is the "partial" electron density of the surface (at the tip-to-surface distance r_0) contributed by those electrons with energy e_f, i.e., the highest occupied level for the surface-to-tip tunneling and the lowest unoccupied level for the tip-to-surface tunneling. For metals, e_f is the Fermi level, and the partial electron density refers to the local density of states at the Fermi level. In reality, factors other than the electronic contribution (e.g., the surface-tip interaction, the tip geometry, etc.) can affect an STM image. Nevertheless, an important step toward a proper interpretation of the STM image of a surface is to calculate the partial electron density distribution $\rho(r_0, e_f)$ of the surface.

In atomic force microscopy (AFM), long-range attractive VDW forces and short-range repulsive forces, resulting from the charge overlap between the tip and the surface, act on the AFM cantilever. In the contact mode of operation, which was employed in our study, the deflection of the cantilever is primarily caused by the repulsive forces thereby giving rise to the image contrast of the surface. A brighter spot of the AFM image is related to a stronger repulsive force the tip feels, a greater charge overlap the tip makes with the surface, and hence a higher electron density region of the surface. Thus, the profiles of the interatomic repulsive forces registered by AFM are expected to reproduce the topography of surface atoms. In fact, AFM images with atomic and molecular resolution obtained for surfaces of various compounds are consistent with the atomic or molecular arrangements expected from their bulk crystal structures.[12,13] The CDWs of 1T-TaX_2 (X = S, Se) were also studied by AFM.[14,15] Since AFM does not require any electron tunneling, it can be used to probe the surface of even an insulator, to which STM is not applicable. Studies of conducting materials by AFM give the topographic information of their surfaces, thereby helping interpret the associated STM images, but AFM often fails to show local surface defects frequently observed by STM. The latter leads one to

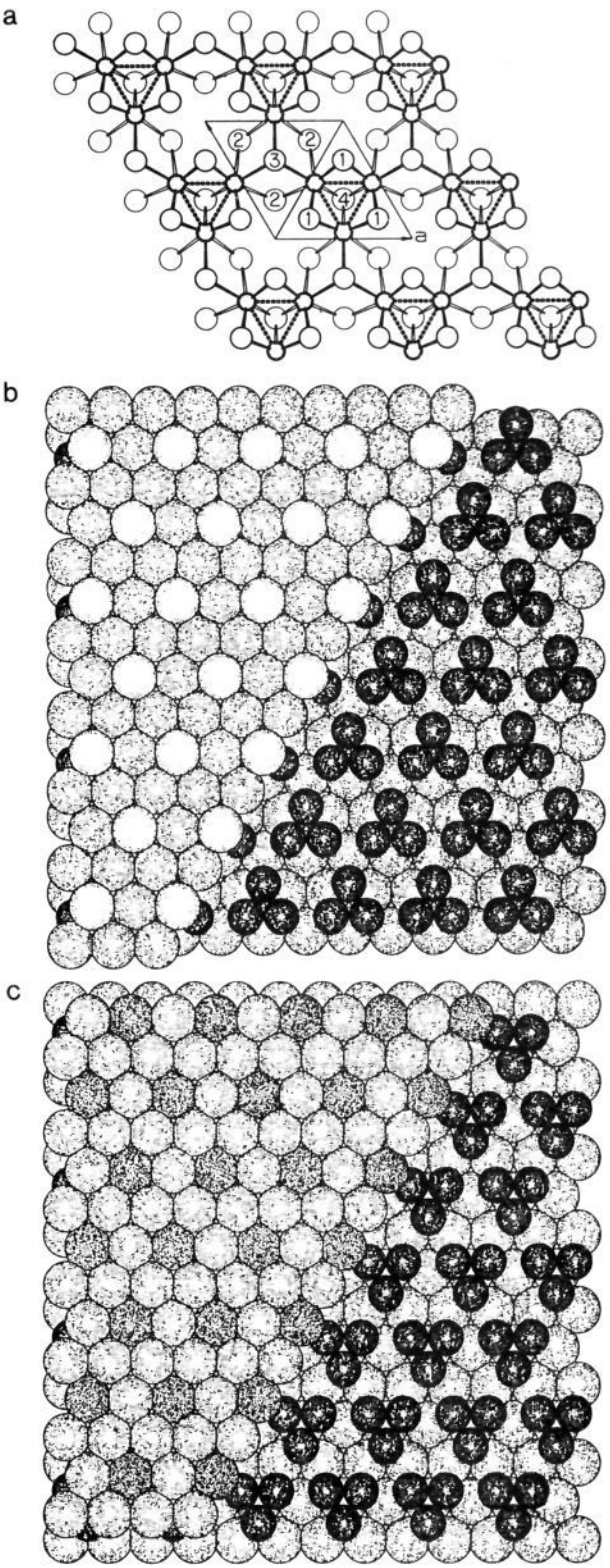

Figure 1. (a) Schematic projection view, along the crystallographic *c*-axis direction, of a single Nb_3X_8 layer. The Nb and X atoms are represented by small and large circles, respectively. The Nb_3 clusters in the Nb atom sheet were shown by connecting the Nb atoms with dashed lines. (b) Schematic projection view of surface A [i.e., the X atom sheet containing the X(2) and X(4) atoms]. The protruded atoms X(4) were shown by a brighter contrast, and a part of the surface X atoms were removed to show the Nb atom clusters (black balls). (c) Schematic projection view of surface B [i.e., the X atom sheet containing the X(1) and X(3) atoms]. The protruded atoms X(1) were shown by a brighter contrast, and a part of the surface X atoms were removed to show the Nb atom clusters (black balls).

(1) Binnig, G.; Rohrer, H.; Gerber, Ch.; Weibel, E. *Phys. Rev. Lett.* **1982**, *49*, 57.
(2) For recent reviews, see: (a) Hansma, P. K.; Tersoff, J. *J. Appl. Phys.* **1987**, *61*, R1. (b) Tromp, R. M. *J. Phys. Cond. Matter* **1989**, *1*, 10211. (c) *Scanning Tunneling Microscopy I and II*; Wiesendanger, R., Güntherodt, H.-J., Eds.; Springer Verlag: Heidelberg, 1992.
(3) Binnig, G.; Quate, C. F.; Gerber, Ch. *Phys. Rev. Lett.* **1985**, *55*, 394.
(4) Ruger, D.; Hansma, P. K. *Physics Today* **1990** (October), 23.
(5) Coleman, R. V.; Drake, B.; Hansma, P. K.; Slough, G. *Phys. Rev. Lett.* **1985**, *55*, 394.
(6) Stupian, G. W.; Leung, M. S. *Appl. Phys. Lett.* **1987**, *51*, 1560.
(7) Akari, S.; Stachel, M.; Birk, H.; Schreck, E.; Lux, M.; Dransfeld, K. *J. Microsc.* **1988**, *152*, 521.
(8) Lieber, C. M.; Xu, X. L. *Acc. Chem. Res.* **1991**, *24*, 170.
(9) Coleman, R. V.; Giambattista, B.; Hansma, P. K.; Johnson, A.; McNairy, W. W.; Slough, C. G. *Adv. Phys.* **1988**, *37*, 559.
(10) Tersoff, J. In *Scanning Tunneling Microscopy and Related Techniques*; Behm, J., Garcia, N., Rohrer, H., Eds.; Kluwer Academic Publishers: Dordrecht, The Netherlands, 1990; p 77.
(11) (a) Tekman, E.; Cirai, S. *Phys. Rev. B* **1989**, *40*, 10286. (b) Ciraci, S.; Baratoff, A.; Batra, I. P. *Phys. Rev. B* **1990**, *41*, 2763.
(12) Drake, B.; Prater, C. B.; Weisenhorn, A. L.; Gould, S. A. C.; Albrecht, T. R.; Quate, C. F.; Cannell, D. S.; Hansma, P. K. *Science* **1989**, *243*, 1586.
(13) Stocker, W.; Bar, G.; Kunz, M.; Möller, M.; Magonov, S. N.; Cantow, H.-J. *Polym. Bull.* **1991**, *26*, 215.
(14) Barrett, R. C.; Nogami, J.; Quate, C. F. *Appl. Phys. Lett.* **1990**, *57*, 992.
(15) Slough, C. G.; McNairy, W. W.; Coleman, R. V.; Garnaes, J.; Prater, C. B.; Hansma, P. K. *Phys. Rev. B* **1990**, *42*, 9255.

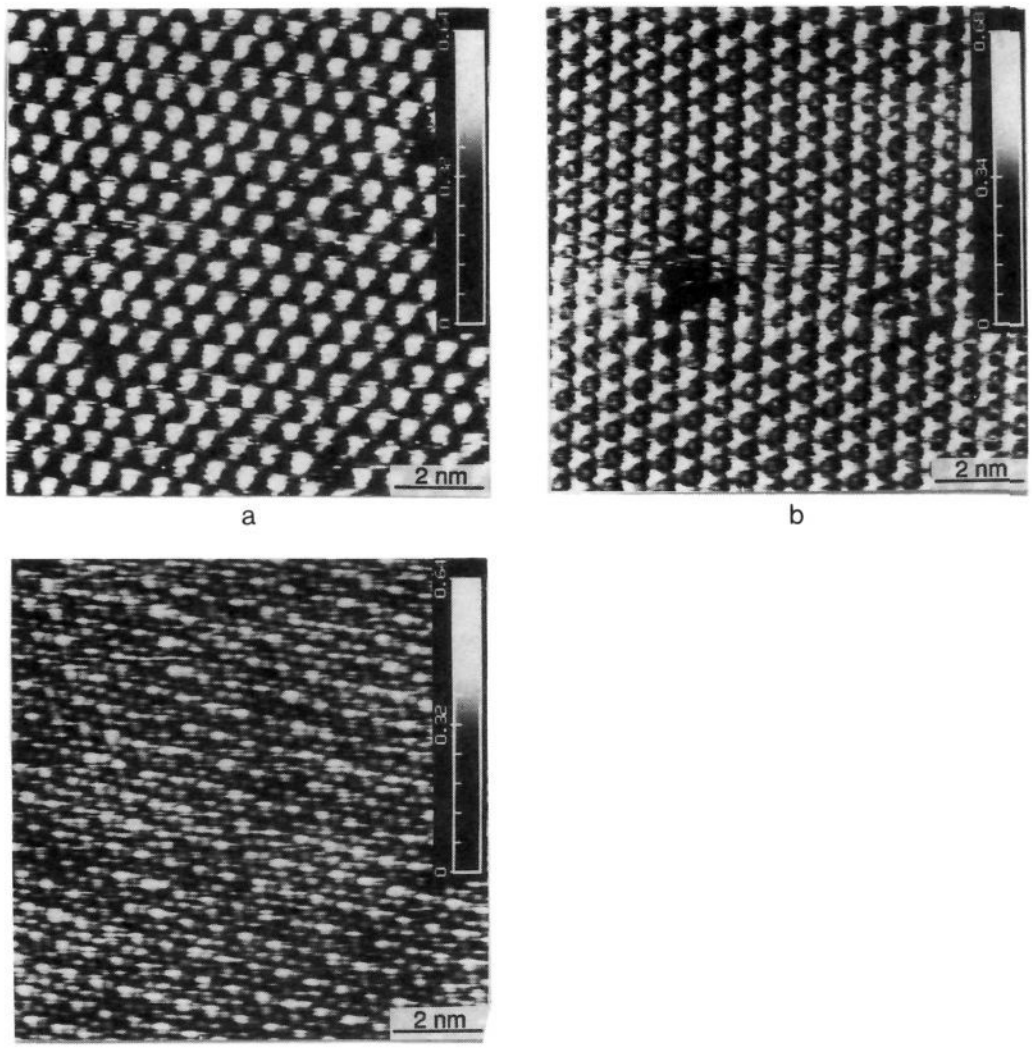

Figure 2. STM and AFM images of β-Nb_3I_8: (a) STM current image recorded at V_{bias} = 1000 mV and I_{tun} = 10 nA. (b) STM current image recorded at V_{bias} = 180 mV and I_{tun} = 0.75 nA. (c) AFM height image. Each vertical gray-scale bar indicates the image variation in relative units proportional to ln(I) for the STM images, where I is the tunneling current, and the image corrugation in nanometers for the AFM image.

Table I. Unit Cell Parameters of Nb_3X_8 (X = Cl, Br, I) Determined by Single-Crystal X-ray Diffraction[24-26] and by AFM and STM Measurements[a]

compd	method	a	c	α
α-Nb_3Cl_8	X-ray	6.744	12.268	120.0
	AFM	7.07 ± 0.67		119.2 ± 2.2
	STM	7.14 ± 0.29		122.5 ± 2.7
β-Nb_3Br_8	X-ray	7.080	38.975	120.0
	AFM	7.23 ± 0.32		122.7 ± 4.1
	STM	7.40 ± 0.17		119.2 ± 2.5
β-Nb_3I_8	X-ray	7.600	41.715	120.0
	AFM	7.73 ± 0.31		120.3 ± 1.7
	STM	7.76 ± 0.43		120.3 ± 2.0

[a] The distances are in Å, and the angles are in deg.

question whether or not AFM is a genuine local-probe technique. Although the exact mechanism of AFM imaging is not clear, it is reasonable to assume that the total electron density of the surface, $\rho(r_0)$, is involved in the interactions of the surface with the tip.

Recently, the STM images of several layered materials have been analyzed on the basis of the $\rho(r_0, e_f)$ plots calculated for their layers by employing the extended Hückel tight-binding (EHTB) electronic band structure method.[16] Being semiempirical in nature, this method has certain limitations. Nevertheless, for several layered inorganic compounds [e.g., $ReSe_2$,[17] $NbSe_3$,[18] α-$RuCl_3$,[19] 1T-TaX_2 (X = S, Se)[20]], the $\rho(r_0, e_f)$ plots calculated by this method are in amazingly good agreement with the observed STM images. In the case of α-$RuCl_3$, for example, the observed "distortion" of the atomic-resolution STM image[21] was found to reflect the partial density distribution, in which the contributions of the Cl p orbitals are not isotropic. The AFM image of α-$RuCl_3$ shows[22] that the surface atom arrangement has a trigonal symmetry, as expected from the X-ray crystal structure. These examples demonstrate that a rational interpretation of STM and AFM images can be achieved on the basis of $\rho(r_0, e_f)$ and $\rho(r_0)$ calculations. In the present work, we examine the surfaces of layered niobium halides Nb_3X_8 (X = Cl, Br, I) by STM and AFM and analyze the observed images by calculating the $\rho(r_0, e_f)$ and $\rho(r_0)$ plots of their single Nb_3X_8 layers. At ambient conditions,

(16) Whangbo, M.-H.; Hoffmann, R. *J. Am. Chem. Soc.* **1978**, *100*, 6093.
(17) Parkinson, B. A.; Ren, J.; Whangbo, M.-H. *J. Am. Chem. Soc.* **1991**, *113*, 7833.
(18) Ren, J.; Whangbo, M.-H. *Phys. Rev. B* **1992**, *46*, 4917.
(19) Ren, J.; Whangbo, M.-H.; Bengel, H.; Magonov, S. N. *J. Phys. Chem.*, submitted for publication.
(20) Whangbo, M.-H.; Ren, J.; Canadell, E.; Louder, D.; Parkinson, B. A.; Bengel, H.; Magonov, S. N. *J. Am. Chem. Soc.*, in press.
(21) Cantow, H.-J.; Hillerbrecht, H.; Magonov, S. N.; Rotter, H.-W.; Drechsler, M.; Thiele, G. *Angew. Chem., Int. Ed. Engl.* **1990**, *29*, 537.
(22) (a) Gould, S. A. C.; Drake, B.; Prater, C. B.; Weisenhorn, A. L.; Manne, S.; Keldermann, G. L.; Butt, H.-J.; Hansma, H.; Hansma, P. K.; Magonov, S. N.; Cantow, H.-J. *Ultramicrosc.* **1990**, *22*, 93. (b) Magonov, S. N. *Appl. Spectrosc. Rev.*, submitted for publication.

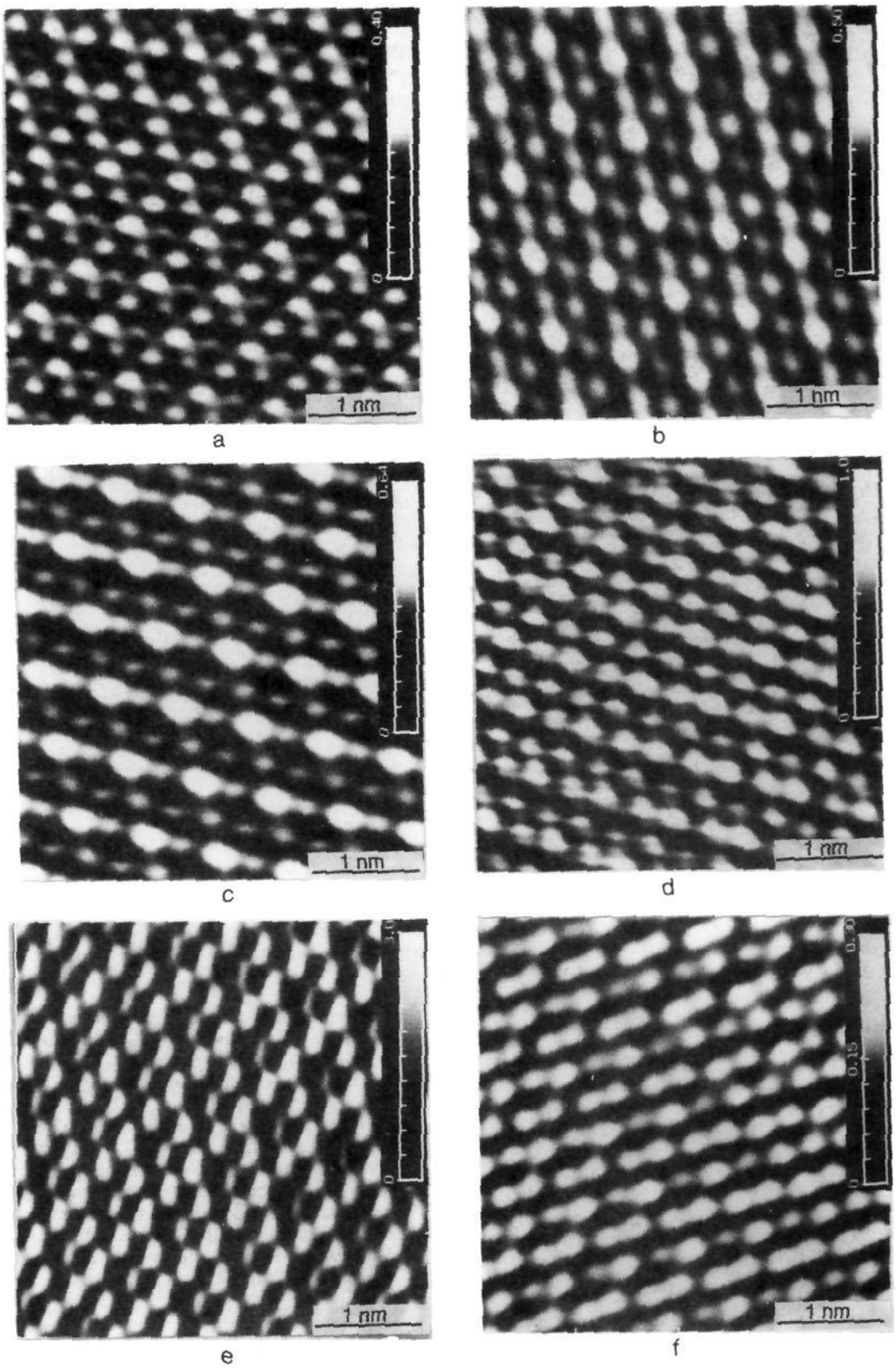

Figure 3. Filtered AFM images of β-Nb_3I_8: (a–c) Successive images recorded for a crystal sample. (d–f) Images recorded for another crystal sample at different rotation angles (0, 120, and 270°, respectiveley) of the sample with respect to the scanning direction. The force imaging mode was used for (e), and the height imaging mode for the rest. Each vertical gray-scale bar indicates the image corrugation in nanometers for the height imaging mode, and the force variation in nN for the force imaging mode.

the electrical conductivities of Nb_3X_8 (ca 10^{-4} Ohm^{-1} cm^{-1})[23] are relatively low but sufficient enough for STM experiments. Thus, the surfaces of these crystals can be studied by both STM and AFM. The Nb_3X_8 layers possess nontrivial structural and electronic features due to the clustering of the Nb atoms into Nb_3 triangles (see Figure 1). All these aspects of Nb_3X_8 are attractive for STM and AFM studies.

(23) Kelert, D. L.; Marshall, R. E. *J. Less-Common Met.* **1974**, *34*, 153.

Table II. Exponents ζ_i and the Valence Shell Ionization Potentials $\mathcal{H}_{ii}$ for Slater type Atomic Orbitals χ_i[a,b]

χ_i	ζ_i	ζ_i'	$\mathcal{H}_{ii}$ (eV)
Br 4s	2.588		−22.1
Br 4p	2.131		−13.1
I 5s	2.679		−18.0
I 5p	2.322		−12.7
Nb 5s	1.89		−10.1
Nb 5p	1.85		−6.86
Nb 4d	4.08 (0.6401)	1.64 (0.5516)	−12.1

[a] $\mathcal{H}_{ii}$'s are the diagonal matrix elements $\langle\chi_i|\mathcal{H}^{eff}|\chi_i\rangle$, where $\mathcal{H}^{eff}$ is the effective Hamiltonian. In our calculations of the off-diagonal matrix elements $\mathcal{H}_{ij} = \langle\chi_i|\mathcal{H}^{eff}|\chi_j\rangle$, the weighted formula was used.[33] [b] The 4d orbitals of Nb are given as a linear combination of two different Slater type orbitals, and each is followed by the weighting coefficient in parentheses.

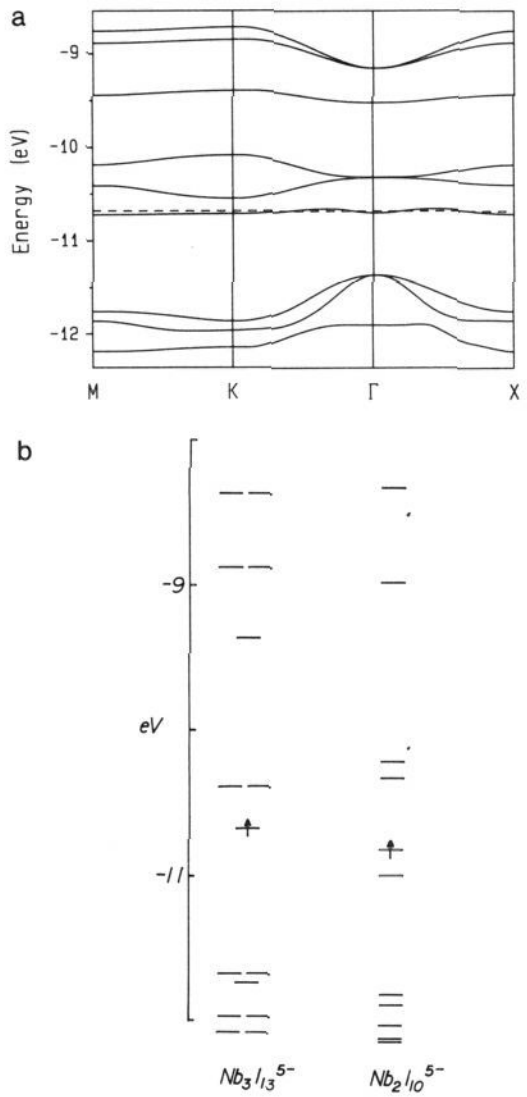

Figure 4. (a) Dispersion relations of the nine bands, in the vicinity of the Fermi level (shown by the dashed line), calculated for a single Nb_3I_8 layer of β-Nb_3I_8. $\Gamma = (0, 0)$, $X = (a^*/2, 0)$, $K = (a^*/3, b^*/3)$, $M = (a^*/2, b^*/2)$. (b) Low-lying energy levels of an $Nb_3I_{13}^{5-}$ cluster and the $Nb_2I_{10}^{5-}$ cluster derived from $Nb_3I_{13}^{5-}$ by deleting one Nb atom and the resulting three dangling I atoms. For the simplicity of presentation, only the highest occupied levels are shown to have electrons.

Experimental Section

A direct reaction between elements readily yields NbX_5, which is then reacted with a stoichiometric amount of metallic niobium at higher temperatures to form Nb_3X_8. Purification and crystallization via chemical transport at 790–810 °C leads to thin black platelike crystals.[24,25]

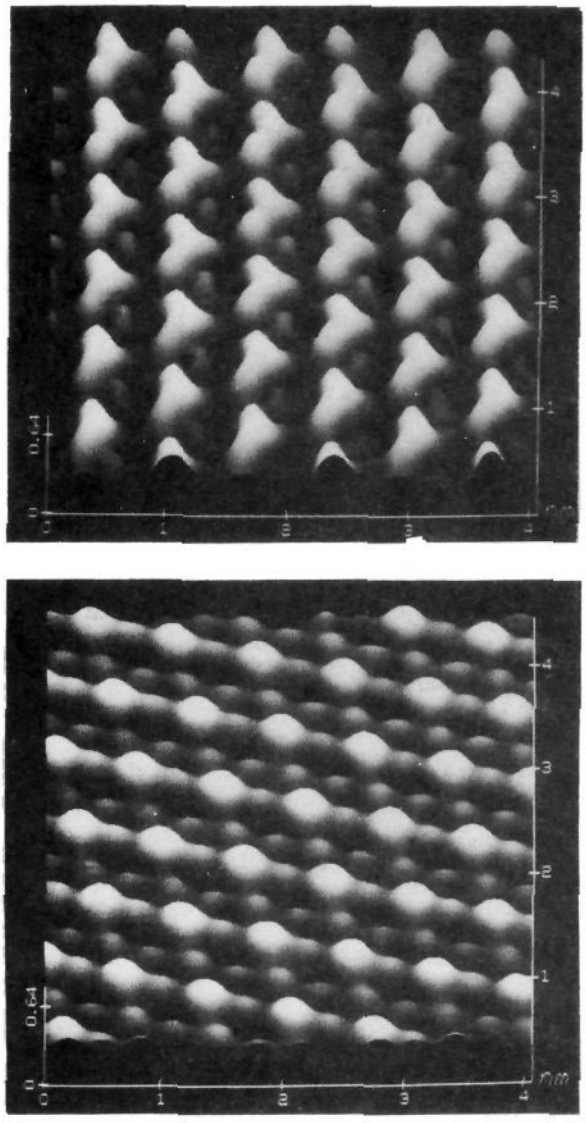

Figure 5. (a) A zoomed and filtered part of the STM current image (three-dimensional surface view) of Figure 2b. (b) A zoomed and filtered part of the AFM height image (three-dimensional surface view) of Figure 3c.

The crystal structures of α-Nb_3Cl_8[24,26] and β-Nb_3X_8 (X = Br, I)[25,26] are all known. The crystal structures of Nb_3X_8 were confirmed on the basis of single-crystal X-ray diffraction measurements by using a CAD 4-diffractometer (Nonius) and the program SHELXTL.[27] For the presentation of the crystal structures, the molecular modeling software SCHAKAL[28] was used.

STM and AFM measurements of β-Nb_3X_8 (X = Br, I) and α-Nb_3Cl_8 were carried out with a commercial scanning probe microscope, Nanoscope II, at ambient conditions. Imaging was conducted with the A scanners. We used mechanically sharpened Pt/Ir (70:30) tips for STM and standard Si_3N_4 probes on the cantilevers with a force constant 0.12 N/m for AFM. Nb_3X_8 crystals were fixed on a copper support by conducting silver glue and were positioned in a similar manner on stages of both STM and AFM.

Since the electrical conductivities of the Nb_3X_8 crystals were relatively low, traces of conducting silver glue were deposited on the freshly cleaved surface in order to improve contact. Even under this condition, the set tunneling current (I_{tun}) and bias voltage (V_{bias}) depend on the distance

(24) Schäfer, H.; von Schnering, H. G. *Angew. Chem.* **1964**, *76*, 833.
(25) Simon, A.; von Schnering, H. G. *J. Less Common Met.* **1966**, *11*, 31.
(26) Hulliger, F. *Structural Chemistry of Layer-Type Phases*; Lévy, F., Ed.; Reidel: Dordrecht, The Netherlands, 1976; p 319.
(27) Siemens Analytical Instrument, program SHELXTL PC, Madison, WI 53719.
(28) Keller, E. J. *Appl. Cryst.* **1989**, *22*, 19.

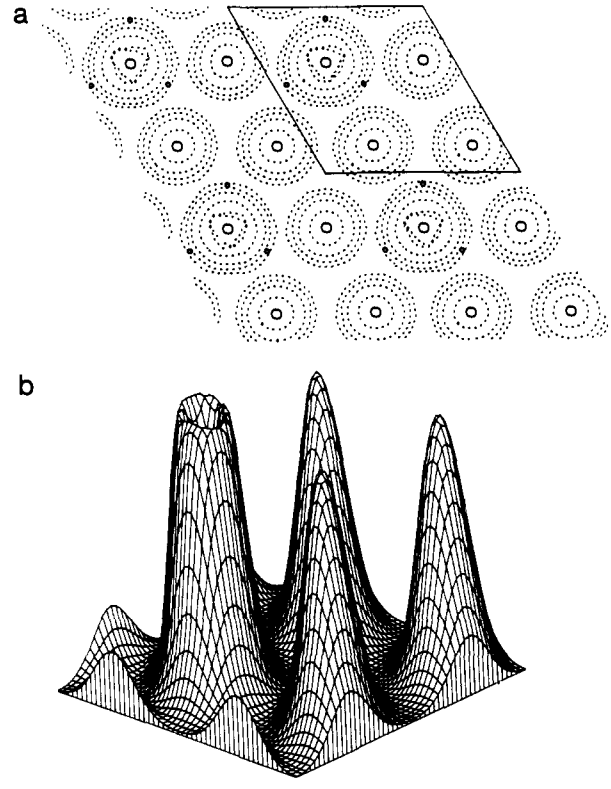

Figure 6. $\rho(r_0)$ plots calculated for surface A of a single Nb_3I_8 layer of β-Nb_3I_8: (a) two-dimensional contour representation. The plot area consists of four unit cells, and a unit cell is indicated by a rhombus. The contour values used are 85, 50, 20, 10, and 5×10^{-3} electrons/au^3. For clarity, the I atoms on the opposite surface are not shown. The Nb and I atoms are shown by small and large circles, respectively. (b) Three-dimensional surface representation: The plot area consists of one unit cell.

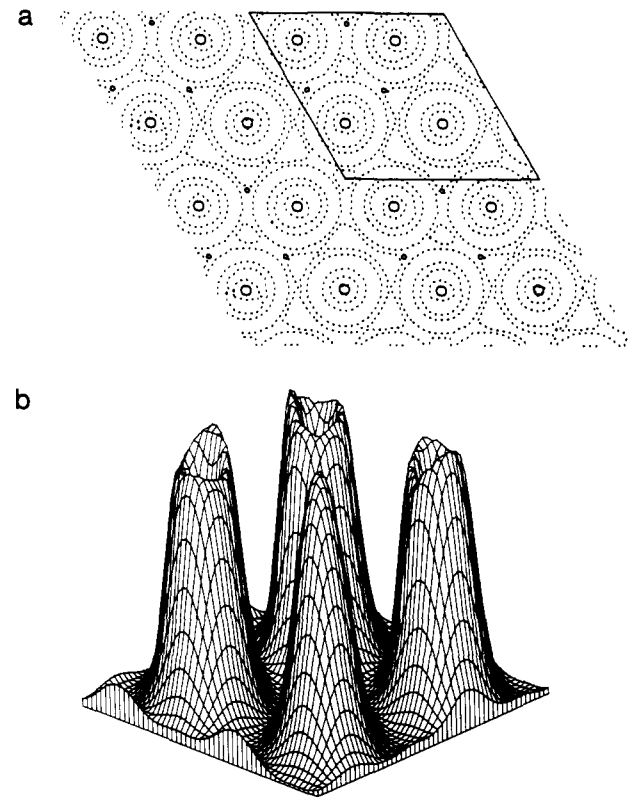

Figure 7. $\rho(r_0)$ plots calculated for surface B of a single Nb_3I_8 layer of β-Nb_3I_8: (a) two-dimensional contour representation. The plot area consists of four unit cells, and a unit cell is indicated by a rhombus. The contour values used are 100, 80, 50, 10, and 5×10^{-3} electrons/au^3. For clarity, the I atoms on the opposite surface are not shown. The Nb and I atoms are shown by small and large circles, respectively. (b) Three-dimensional surface representation: The plot area consists of one unit cell.

from a surface electric contact to the imaging spot due to a voltage drop in the low conductive surface. It was possible to obtain STM images at both plus and minus bias voltages in the range of 10 mV to 2 V. The voltage-current curves at different bias voltages are similar, which indicates a metallic character of the Nb_3X_8 crystals. The tunneling current was varied in the range of 0.7–35 nA. The line scanning frequency during measurements on a small area (less than 20×20 nm^2) was in the range of 19–78 Hz.

STM and AFM images were registered in two different modes. With high feedback parameters, the height imaging mode was used to obtain the three-dimensional maps of the surface image. With low feedback parameters, the surface was scanned with the tip at a constant height over the sample, so that the variation of current was visualized in the STM images and that of force in the AFM images. An important feature of AFM is the ability to change the scanning direction with respect to the sample, and we collected AFM images at different rotation angles.

During the STM and AFM measurements of Nb_3X_8, etching of the surface layers was observed. Similar observations were made earlier on other compounds.[29,30] The etching effect was more frequently found in the STM measurements for β-Nb_3Br_8 and α-Nb_3Cl_8 than for β-Nb_3I_8. When etching occurs, the observed atomic-scale images are not associated with the surface layer but with a lower lying layer. This can lead to difficulties in the comparison of STM and AFM images if a given compound consists of several different types of surfaces.

To accentuate the periodic features of STM and AFM images, filtering was applied to our data by employing the two-dimensional fast fourier transform (FFT) procedure. The most pronounced spots in the power spectrum resulting from the FFT procedure were saved for the restoration of the idealized image in the inverse process. The parameters of STM and AFM images, recorded at various scanning and rotation directions, were averaged to minimize the influence of thermal drift.

Crystal Structures of Nb_3X_8 (X = Cl, Br, I). Nb_3X_8 (X = Cl, Br, I) is made up of identical Nb_3X_8 layers. In a single Nb_3X_8 (X = Cl, Br, I) layer (Figure 1a), a sheet of Nb atoms is sandwiched between sheets of X atoms. In the Nb atom sheet, the Nb atoms form triangular Nb_3 clusters, so that each Nb atom is under a distorted octahedral environment. It is noted that an Nb_3X_8 layer can be regarded as derived from Nb_3X_{13} clusters (**1**) by sharing their octahedral edges. β-Nb_3X_8 (X = Br, I) has six Nb_3X_8 layers per unit cell, while α-Nb_3Cl_8 has two Nb_3Cl_8 layers per unit cell.[24-26] The unit cell parameters of Nb_3X_8 (X = Cl, Br, I) are summarized in Table I.

In each Nb_3X_8 layer, the top and bottom sheets of X atoms are not equivalent. On the bottom sheet of X atoms containing the X(2) and X(4) atoms in Figure 1a (hereafter, referred to as surface A), the X(4) atoms lie farther away from the Nb atom sheet than are the X(2) atoms by 0.60, 0.55, and 0.50 Å for X = I, Br, and Cl, respectively. On the top sheet of X atoms containing the X(1) and X(3) atoms in Figure 1a (hereafter, referred to as surface B), the X(1) atoms lie farther away from the Nb atom sheet than are the X(3) atoms by 0.44, 0.33, and 0.35 Å for X = I, Br, and Cl, respectively. Schematic projection views of surfaces A and B are shown in Figure 1, parts b and c, respectively. In principle, the surfaces of Nb_3X_8 (X = Cl, Br, I) samples can be either surface A or B. Thus, in the interpretation of the STM and AFM images, it is essential to know whether they are associated with surface A or B.

STM and AFM Images. The most representative STM and AFM images of β-Nb_3I_8 are shown in Figures 2a–c. The main features of these images are also found in the STM and AFM images of β-Nb_3Br_8 and α-Nb_3Cl_8 (Figures 11 and 12). These STM and AFM images can be characterized by the surface unit cell parameters a_{STM} and a_{AFM}, respectively, under the assumption that their patterns have a trigonal symmetry as do the crystal structures of the individual Nb_3X_8 layers. As summarized in Table 1, the a_{STM} and a_{AFM} values agree well with the corresponding values of the bulk crystal structures.

The STM images with one big bright spot per unit cell (Figure 2a) were obtained frequently. In many cases, changing the tunneling parameters to a smaller tunneling gap resistance (i.e., V_{bias}/I_{tun}) leads to a more resolved STM image with four patterns per unit cell (See Figure 2b. For a zoomed and filtered part of this image, see Figure 5a.), which consist of three brighter triangular spots and a less pronounced spot. The STM images exhibit large defects (of approximately the size of three

(29) Parkinson, B. A. *J. Am. Chem. Soc.* **1990**, *112*, 7498.
(30) Delawski, E.; Parkinson, B. A. *J. Am. Chem. Soc.* **1992**, *114*, 1661.

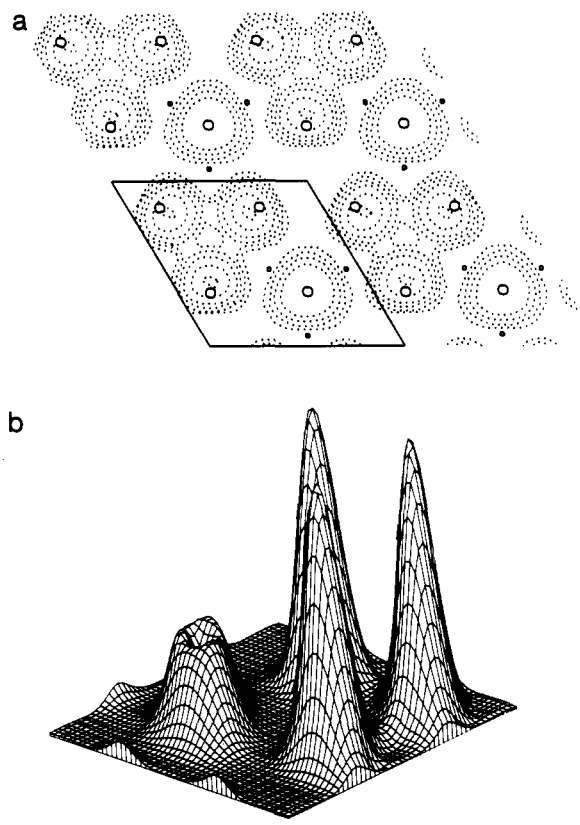

Figure 8. $\rho(r_0, e_f)$ plots calculated for surface A of a single Nb_3I_8 layer of β-Nb_3I_8: (a) two-dimensional contour representation. The plot area consists of four unit cells, and a unit cell is indicated by a rhombus. The contour values used are 100, 50, 20, 15, 5, and 2×10^{-5} electrons/au^3. For clarity, the I atoms on the opposite surface are not shown. The Nb and I atoms are shown by small and large circles, respectively. (b) Three-dimensional surface representation: The plot area consists of one unit cell.

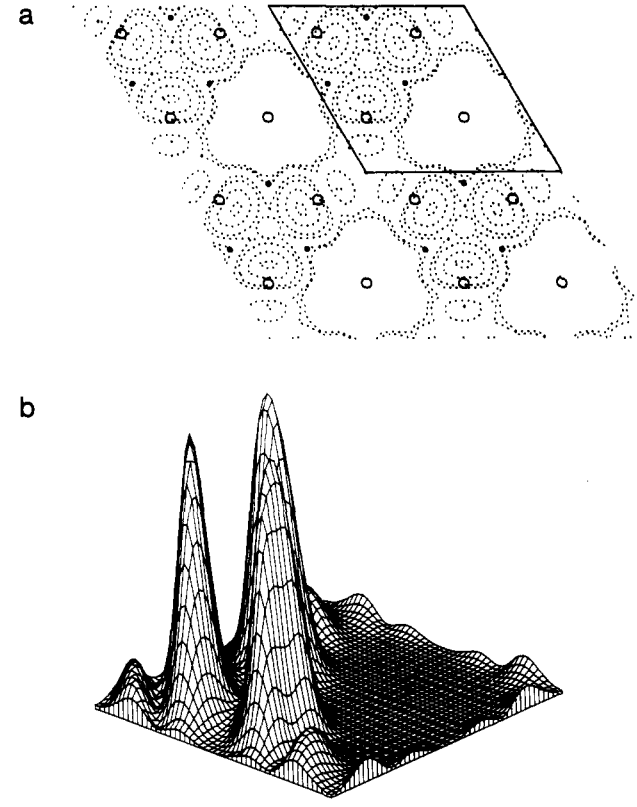

Figure 9. $\rho(r_0, e_f)$ plots calculated for surface B of a single Nb_3I_8 layer of β-Nb_3I_8: (a) two-dimensional contour representation. The plot area consists of four unit cells, and a unit cell is indicated by a rhombus. The contour values used are 600, 300, 100, 50, 10, and 5×10^{-5} electrons/au^3. For clarity, the I atoms on the opposite surface are not shown. The Nb and I atoms are shown by small and large circles, respectively. (b) Three-dimensional surface representation: The plot area consists of one unit cell.

triangular spots) (see Figures 2a,b and 11b). Atomic resolution AFM images were obtained for β-Nb_3I_8 (Figure 2c), but such large defects as observed in the STM images were not found in the AFM images. This phenomenon has also been observed for other layered inorganic compounds such as 1T-TaX_2 (X = S, Se)[9] and organic conducting salts.[31] The AFM images observed at different force levels and at different rotation angles do not exhibit strong changes, and all AFM images exhibit four patterns per unit cell.

The differences in the heights of the AFM height images were in the range of 0.5–1.2 Å, close to the atomic corrugations in surfaces A and B. Variations in the "height-contrast" were observed in successive AFM images recorded without changing the rotation angle (Figures 3a–c) as well as in those registered at different rotation angles (Figures 3d–f). The contrast variations in the images of Figures 3a–c are due probably to the instabilities of the contact between the probe and the surface. The atomic arrangement of the surface Nb_3X_8 layer is not likely to have a symmetry lower than the trigonal symmetry expected from the bulk structure. Therefore, it is probable that the lower symmetry contrast of the observed AFM images is caused by a nonideal geometry of the tip. This interpretation is consistent with the finding that the contrast variations depend on the rotation angles. Therefore, in the present work, we assume that the true topography of the surface is represented by the most symmetrical AFM images (in the sense of contrast). In fact, such images with the unit patterns consisting of one higher spot surrounded by three smaller spots were recorded frequently.

Calculations

Since the individual layers of most layered transition-metal compounds are held by VDW interactions, the structures of the surface layers should be practically identical with those of the layers in the bulk. Thus, we calculate the $\rho(r_0)$ and $\rho(r_0, e_f)$ plots of single Nb_3X_8 (X = Cl, Br, I) layers on the basis of their electronic structures calculated by the EHTB method. The atomic parameters employed for our EHTB calculations are summarized in Table II.

The dispersion relations of the energy bands calculated for a single Nb_3I_8 layer (nine bands lying in the vicinity of the Fermi level) are shown in Figure 4a. With the oxidation state I^-, there are seven electrons to fill the bottom four bands of Figure 4a so that the highest occupied band, which is somewhat narrow, is half filled. In the absence of electron localization, this predicts metallic character for β-Nb_3I_8. The magnetic susceptibility of β-Nb_3I_8 exhibits a nearly constant paramagnetism between 90 and 350 K,[25] which is indicative of metallic character. In essence, the band electronic structure calculated for a single Nb_3X_8 (X = Cl, Br) layer is similar to that of a single Nb_3I_8 layer shown in Figure 4a (hence not shown).

The energy levels of the $Nb_3I_{13}^{5-}$ cluster **1** calculated by the extended Hückel method are shown in Figure 4b. The energy bands of Figure 4a are derived largely from these levels of each $Nb_3I_{13}^{5-}$ cluster. In particular, the highest occupied band is derived from the highest occupied molecular orbital (HOMO) of each cluster.

In our calculations of $\rho(r_0)$ and $\rho(r_0, e_f)$, the r_0 value was taken to be 0.5 Å (i.e., 0.5 Å away from the atoms closest to the tip). The orbital amplitudes of the wave functions of a surface decrease exponentially with distance from the surface, so that the $\rho(r_0, e_f)$ values become too small for meaningful comparisons if r_0 is much greater than 0.5 Å. The values calculated for r_0 = 0.5 Å have been found to accurately reflect the tunneling probabilities from a more distant tip for many layered materials.[17-20,32] In addition, we notice that, in a simultaneous STM/AFM study of 1T-TaS_2 at ambient conditions,[14] the STM image obtained with the tip in contact with the surface is nearly identical with that registered

(31) Magonov, S. N.; Bar, G.; Cantow, H.-J.; Laukhin, V. N.; Yagubskii, E. B. *Synth. Met.*, submitted for publication.

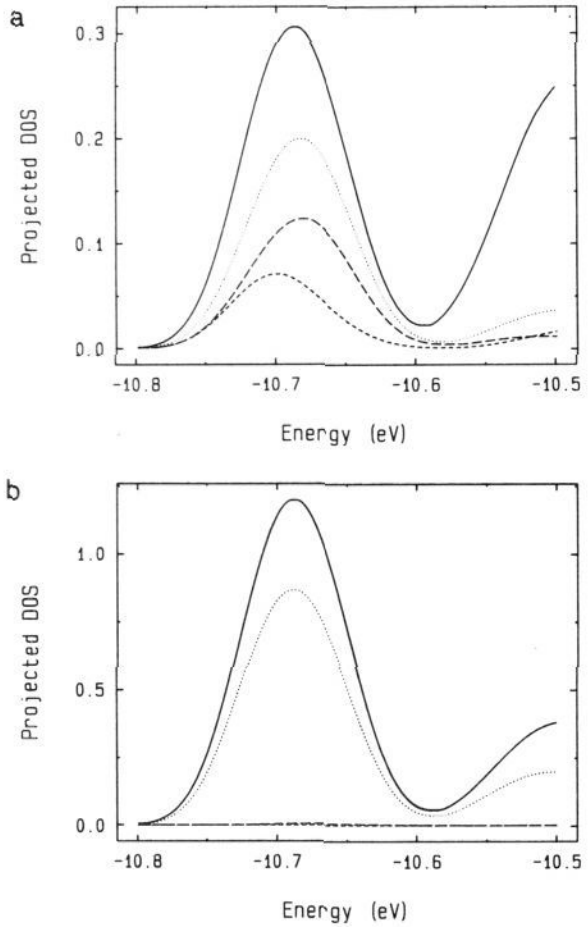

Figure 10. Projected DOS values of the iodine atoms, in the energy region of the half-filled band, calculated for a single Nb_3I_8 layer of β-Nb_3I_8. (a) The iodine atoms of surface A: the p_z orbital of I(2) [dotted line], the p_x and p_y orbitals of I(2) [solid line], the p_z orbital of I(4) [short-dash line], and the p_x and p_y orbitals of I(4) [long-dash line]. (b) The iodine atoms of surface B: the p_z orbital of I(1) [dotted line], the p_x and p_y orbitals of I(1) [solid line], the p_z orbital of I(3) [short-dash line], and the p_x and p_y orbitals of I(3) [long-dash line].

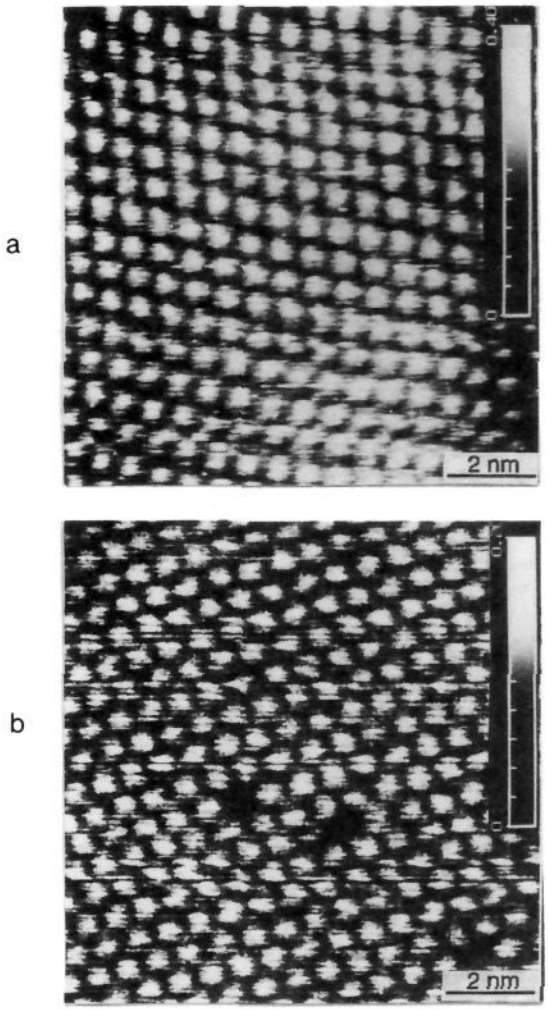

Figure 11. (a) STM current image of β-Nb_3Br_8 recorded at V_{bias} = −397 mV and I_{tun} = 1 nA. (b) STM current image of β-Nb_3Cl_8 recorded at V_{bias} = 539 mV and I_{tun} = 1 nA. Each vertical gray-scale bar indicates the image variation in relative units proportional to ln(I).

in a traditional STM study. Consequently, the $\rho(r_0, e_f)$ plot calculated for a small r_0 value can be used for the interpretation of the STM images.

Interpretation of the STM and AFM Images. The STM and AFM images of β-Nb_3I_8, registered on a same sample surface, were chosen for our analysis. In Figure 5a,b, the periodical features of these images are emphasized by filtering. Layered compounds usually give well-resolved STM and AFM images, and their patterns correlate well with the crystallographic unit cell parameters. However, few examples show such striking differences in their STM and AFM images as those found for β-Nb_3I_8. On the basis of the experimental images alone, it is difficult to determine whether they are associated with surface A or surface B.

The $\rho(r_0)$ plots of a single Nb_3I_8 layer calculated for surface A are shown in Figure 6, and those for surface B in Figure 7. In each unit cell of the $\rho(r_0)$ plot for surface A (Figure 6), one atom *[i.e., I(4)] has a greater density than do three other atoms [i.e.,* I(2)'s]. In each unit cell of the $\rho(r_0)$ plot for surface B (Figure 7), however, three atoms [i.e., I(1)'s] have a greater density than does the remaining atom [i.e., I(3)]. Consequently, the observed AFM image (Figure 5b) is consistent with the $\rho(r_0)$ plot of surface A. The experimental image variations described above (Figure 3) may cast some doubt on this assignment, but it is fully supported by the analysis of the STM image discussed below.

The $\rho(r_0, e_f)$ plots of a single Nb_3I_8 layer calculated for surface A are shown in Figure 8, and those for surface B in Figure 9. These plots were obtained by sampling all levels of the half-filled band of Figure 4a. The $\rho(r_0, e_f)$ plots calculated by sampling only those energy levels lying within a small energy window (e.g., 0.1 eV) from the Fermi level are essentially the same as those shown Figures 8 and 9. This is so because the orbital compositions of the half-filled band are nearly uniform throughout the band as shown by Figure 10, which plots the projected density of states (DOS) of the four different iodine atoms in the energy region of the half-filled band. In the $\rho(r_0, e_f)$ plot of surface A (Figure 8), the I(2) atoms have a greater density than do the I(4) atoms despite the fact that the I(2) atoms lie farther away from the tip by 0.60 Å. This is due to the fact that the highest occupied band has a greater contribution from the I(2) atoms than from the I(4) *atoms (see Figure 10a). Figure 8 shows that the density peaks* of the three I(2) atoms in a unit cell are closer to one another than expected on the basis of the crystal structure. This is caused by the hybridization of the I(2) atom p-orbitals in the half-filled band. Figure 10a shows that the projected DOS of I(2) has contributions from both the out-of-plane p-orbital (i.e., the p_z-orbital) and the in-plane p-orbitals (i.e., the p_x and p_y-orbitals). The STM current image of Figure 5a exhibits triangular bright spots. When these spots are not resolved by STM measurements, they appear as a big bright spot as shown in Figure 2a. The I(4) atoms have a

(32) Tang, S. L.; Kasowski, R. V.; Suna, A.; Parkinson, B. A. *Surf. Sci.* **1991**, *238*, 280.
(33) Ammeter, J. H.; Bürgi, H.-B.; Thibeault, J.; Hoffmann, R. *J. Am. Chem. Soc.* **1978**, *100*, 3686.

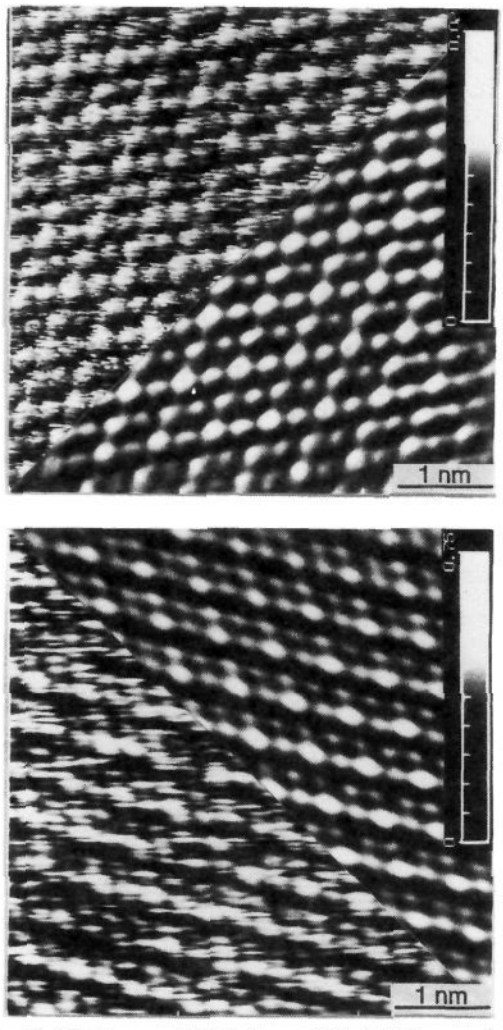

Figure 12. (a) AFM image of β-Nb_3Br_8 and (b) AFM image of α-Nb_3Cl_8. Each vertical scale bars indicate the image corrugation in nanometers.

much smaller density peak than do the I(2) atoms, so that the I(4) atoms should appear as very dim spots. Thus, the $\rho(r_0, e_f)$ plot calculated for surface A is consistent with the observed STM images (Figures 2b and 5a). In the $\rho(r_0, e_f)$ plot calculated for surface B (Figure 9), the I(3) atom contribution is absent because the I(3) atoms lie farther away from the tip than the I(1) atoms by 0.44 Å and also because the projected DOS of I(3) nearly vanishes in the half-filled band region (see Figure 10b).

We now examine a probable cause for the large defects in the STM image of β-Nb_3I_8. This image is primarily determined by the partial electron density associated with the highest occupied band of the surface Nb_3I_8 layer, and the highest occupied band is made up of the HOMO from each $Nb_3I_{13}^{5-}$ cluster. Thus, each bright spot of the STM image represents the electron density given by the HOMO of the corresponding $Nb_3I_{13}^{5-}$ cluster. The tunneling current is sensitive only to the partial electron density associated with the Fermi level. Thus, when an $Nb_3I_{13}^{5-}$ cluster is modified to have a lower lying HOMO than do other $Nb_3I_{13}^{5-}$ clusters, it cannot contribute to a tunneling current and should appear as dark in the STM image as if the whole cluster were missing. Such a situation occurs when a cluster has an Nb atom defect as illustrated in Figure 4b, which compares the energy levels of an $Nb_3I_{13}^{5-}$ cluster with those of an $Nb_2I_{10}^{5-}$ cluster (derived from an $Nb_3I_{13}^{5-}$ cluster by deleting one Nb atom and the resulting three dangling I atoms).

STM and AFM Images of β-Nb_3Br_8 and α-Nb_3Cl_8. The characteristic features of the $\rho(r_0)$ and $\rho(r_0, e_f)$ plots calculated for a single Nb_3Br_8 layer of β-Nb_3Br_8, and also for a single Nb_3Cl_8 layer of α-Nb_3Cl_8, are similar to those of β-Nb_3I_8 (hence not shown). Consequently, the analysis of the AFM and STM images of these compounds can be carried out by referring to the $\rho(r_0)$ and $\rho(r_0, e_f)$ plots in Figures 6–9. The STM images of β-Nb_3Br_8 and α-Nb_3Cl_8, shown in Figure 11a,b, respectively, are frequently observed. These images exhibit one pronounced spot per unit cell, and hence cannot be assigned to surface A or B. Identification of the observed surface requires more resolved details within a unit cell. Some STM images exhibit two patterns (one big and bright, and the other smaller and dim) or four patterns per unit cell. Although this finding supports the assignment of the observed surface to surface A, the quality of such STM images was lower than that shown in Figure 2b.

The AFM images of β-Nb_3Br_8 and α-Nb_3Cl_8 are shown in Figure 12a,b, respectively. They are similar to the images obtained for β-Nb_3I_8 in that a unit cell consists of four spots, and one spot is brighter than the rest. This shows that the images are associated with surface A. The height variations were in the range of 0.5–1.5 Å. The reproducibility of these variations was not good enough for the correlation with the corrugation heights of the surface X atoms, but the surface unit cell parameters derived from the image patterns agree well with the corresponding values of the bulk crystal structures. As in the case of β-Nb_3I_8, the variations of the images were also found during the measurements at different rotation angles.

Concluding Remarks. We obtained atomic-resolution AFM and STM images of layered halides Nb_3X_8 (X = Cl, Br, I) and analyzed them by calculating the $\rho(r_0)$ and $\rho(r_0, e_f)$ plots of single Nb_3X_8 layers. The surfaces of Nb_3X_8 samples can be either surface A or B, but comparison of the experimental AFM images with the calculated $\rho(r_0)$ plots shows that the images observed for the Nb_3X_8 samples are associated with surface A. Our work shows that the AFM and STM images are very well described by the $\rho(r_0)$ and $\rho(r_0, e_f)$ plots, respectively, and that, for the interpretation of AFM and STM images of layered materials, calculations of their $\rho(r_0)$ and $\rho(r_0, e_f)$ plots are indispensable. For a given surface, the topography of the $\rho(r_0, e_f)$ plot is not necessarily the same as that of the $\rho(r_0)$ plot. Thus, one should note that the structure of a surface deduced from an STM analysis, under the typical assumption that bright STM spots represent the surface atomic positions, can be quite misleading.

Acknowledgment. We thank H. Bengel and P. Jeitschko for their participation in the experiments. Work at North Carolina State University was supported by the Office of Basic Energy Sciences, Division of Materials Sciences, U.S. Department to of Energy, under Grant DE-FG05-86ER45259.